

14. A. Dai, T. M. L. Wigley, B. A. Boville, J. T. Kiehl, L. E. Buja, *J. Clim.* **14**, 485 (2001).
15. D. V. Hoyt, K. H. Schatten, *J. Geophys. Res.* **98**, 18895 (1993).
16. G. A. Meehl, W. M. Washington, T. M. L. Wigley, J. M. Arblaster, A. Dai, *J. Clim.* **16**, 426 (2003).
17. C. Ammann, G. A. Meehl, W. M. Washington, C. S. Zender, *Geophys. Res. Lett.* **30**, 1657 (2003) (DOI 10.1029/2003GL016875).
18. The G, A, and O forcings in the PCM experiments are identical to those used in integrations performed with the NCAR Climate System Model (13, 14). Total solar irradiance changes were prescribed according to Hoyt and Schatten (15) and updated as in (16), with no wavelength dependence of the forcing. Volcanic forcing was based on estimates of total sulfate loading and a simplified model of aerosol distribution and decay (17).
19. E. Kalnay *et al.*, *Bull. Am. Meteorol. Soc.* **77**, 437 (1996).
20. J. K. Gibson *et al.*, *ECMWF Re-Analysis Project Reports Series 1* (European Centre for Medium-Range Weather Forecasts, Reading, UK, 1997), 66 pp.
21. S. Pawson, M. Fiorino, *Clim. Dyn.* **15**, 241 (1999).
22. B. D. Santer *et al.*, *J. Geophys. Res.* **104**, 6305 (1999).
23. World Meteorological Organization (WMO), *Meteorology—A Three-Dimensional Science: Second Session of the Commission for Aerology* [WMO Bulletin IV(4), WMO, Geneva, 1957], pp. 134–138.
24. T. Reichler, M. Dameris, R. Sausen, D. Nodorp, *A Global Climatology of the Tropopause Height Based on ECMWF Analyses* (Institut für Physik der Atmosphäre, Report 57, Deutsche Forschungsanstalt für Luft und Raumfahrt, Wessling, Germany, 1996).
25. We estimate p_{LRT} from reanalysis and model data by interpolation of the lapse rate in a p^κ coordinate system, where p denotes pressure, $\kappa = R/c_p$, and R and c_p are the gas constant for dry air and the specific heat capacity of dry air at constant pressure (24). The algorithm identifies the threshold model level at which the lapse rate falls below $2^\circ\text{C}/\text{km}$ and then remains less than this critical value for a specified vertical distance (23). The exact pressure at which the lapse rate attains the critical value is determined by linear interpolation of lapse rates in the layers immediately above and below the threshold level. This definition of tropopause height is robust under most conditions. Exceptions include situations where the atmosphere is relatively isothermal or where multiple stable layers are present (24). To avoid unrealistically high or low p_{LRT} values, search limits are restricted to pressure levels between roughly 550 and 75 hPa. Decadal-scale trends in p_{LRT} are relatively insensitive to the temporal resolution of the input temperature data (3, 6).
26. The NCEP p_{LRT} calculation performed here used monthly mean temperature data at 17 model pressure levels. A similar calculation used the 6-hourly temperature data available at 28 model sigma levels, with higher resolution in the vicinity of the tropical tropopause (6).
27. C. A. Mears, M. C. Schabel, F. W. Wentz, *J. Clim.*, in press.
28. J. R. Christy, R. W. Spencer, W. D. Braswell, *J. Atmos. Ocean. Tech.* **17**, 1153 (2000).
29. The radiative emissions contributing to the T4 and T2 measurements peak at roughly 74 and 595 hPa, respectively. In the tropics, emissions from the troposphere make a substantial contribution to estimated T4 temperatures.
30. B. D. Santer *et al.*, *Science* **300**, 1280 (2003).
31. The total linear change in T4 in NCEP is -1.65°C over 1979–1999 (32). This is considerably larger than the simulated T4 change of -0.73°C in ALL or the estimated observed MSU T4 changes of -0.93°C (27) and -1.07°C (28). NCEP's excessive stratospheric cooling is due to biases in both the satellite-derived temperature retrievals and the assimilated radiosonde data (6, 27). Because T2 receives a small (roughly 10% globally) contribution from the stratosphere, any error in NCEP's T4 trends will propagate into $\Delta T2$. This partly explains why NCEP's troposphere cools markedly over 1979–1999, with a total linear change in T2 of -0.22°C .
32. The total linear change is defined as $b \times n$, where b is the slope parameter of the linear trend (in hPa per month or $^\circ\text{C}$ per month) fitted by the standard least-squares method over a specified period of n months.
33. For forcing component x , this is calculated as $(x/y) \times 100$, where x is the total linear change in p_{LRT} over a stipulated time interval (due to x) and y is the linear change in p_{LRT} (over the same interval) due to ALL. This definition is not applicable if the linear change in ALL is close to zero, a situation that never arises here.
34. V. Ramaswamy, M. D. Schwarzkopf, W. Randel, *Nature* **382**, 616 (1996).
35. Because the O experiment does not separate tropospheric and stratospheric ozone changes, we cannot quantify their individual contributions to overall changes in p_{LRT} . Historical increases in tropospheric ozone are expected to warm T2, thereby increasing tropopause height. Such warming is not evident in the O integration (Fig. 2C) because of the cooling effect of stratospheric ozone depletion on the upper troposphere. Figure 2 indicates that in PCM, ozone-induced increases in tropopause height arise primarily through stratospheric ozone depletion and the resultant cooling of T4, not through tropospheric ozone changes.
36. P. A. Stott *et al.*, *Science* **290**, 2133 (2000).
37. Linear changes in tropopause height over 1979–1999 are the sole exception: SUM results are 19% smaller than in ALL. This difference is largely attributable to noise differences. SUM is a linear combination of five climate responses plus five different (ensemble-averaged) noise estimates, and must therefore be noisier than ALL. ALL versus SUM noise differences are likely to have the greatest impact on trends calculated over relatively short periods.
38. K. Hasselmann, in *Meteorology of Tropical Oceans*, D. B. Shaw, Ed. (Royal Meteorological Society of London, London, UK, 1979), pp. 251–259.
39. B. D. Santer *et al.*, *J. Geophys. Res.* **100**, 10693 (1995).
40. E. Roeckner, L. Bengtsson, J. Feichter, J. Lelieveld, H. Rodhe, *J. Clim.* **12**, 3004 (1999).
41. Two reanalyses (NCEP and ERA) combined with two noise data sets for calculation of natural variability statistics (PCM and ECHAM) yields four nonoptimized detection time estimates.
42. W. J. Randel, F. Wu, W. R. Rios, *J. Geophys. Res.* **108**, 4024 (2003) (DOI 10.1029/2002JD002595).
43. Work at Lawrence Livermore National Laboratory was performed under the auspices of the U.S. Department of Energy (DOE), Environmental Sciences Division, contract W-7405-ENG-48. T.M.L.W. was supported by the National Oceanic and Atmospheric Administration Office of Global Programs (Climate Change Data and Detection) grant no. NA87GP0105 and by DOE grant no. DE-FG02-98ER62601. A portion of this study was supported by the DOE Office of Biological and Environmental Research, as part of its Climate Change Prediction Program. The MSU weighting functions were provided by J. Christy (Univ. of Alabama in Huntsville). E. Roeckner (Max-Planck Institut für Meteorologie, Hamburg, Germany) supplied ECHAM control run data. Review comments from B. Hoskins and S. Pawson substantially improved the manuscript. We also thank R. Anthes, W. Randel, and J. Bates for bringing GPS-based monitoring of tropopause height to our attention.

Supporting Online Material

www.sciencemag.org/cgi/content/full/301/5632/479/

DC1

SOM Text

Fig. S1

4 March 2003; accepted 30 May 2003

Dense Packing and Symmetry in Small Clusters of Microspheres

Vinothan N. Manoharan,¹ Mark T. Elsesser,¹ David J. Pine^{1,2*}

When small numbers of colloidal microspheres are attached to the surfaces of liquid emulsion droplets, removing fluid from the droplets leads to packings of spheres that minimize the second moment of the mass distribution. The structures of the packings range from sphere doublets, triangles, and tetrahedra to exotic polyhedra not found in infinite lattice packings, molecules, or minimum-potential energy clusters. The emulsion system presents a route to produce new colloidal structures and a means to study how different physical constraints affect symmetry in small parcels of matter.

What defines an optimal packing of a set of n identical spheres? Although centuries old, this question remains both pertinent and pervasive in mathematics and science (1). For packings of an infinite number of spheres, the obvious measure of optimality is the bulk density. As Kepler conjectured and Hales proved (2, 3), the optimal infinite packing is the face-centered cubic (fcc) arrangement, which maximizes the density or, equivalently, minimizes the volume per sphere. But for a finite group of spheres there is no compelling definition of density, and optimality in

finite sphere packings can be defined by the minimization of any physically reasonable variable, such as potential energy or surface area, for example. Different minimization criteria can lead to dramatically different sequences of packings (4), with symmetries that are rarely consistent with that of an infinite (bulk) packing.

In nature, differences in symmetry between finite and bulk packings manifest themselves in a variety of phenomena. The interactions between atoms or particles in many systems, including metals, noble gases, and colloids, are nearly spherically isotropic, and the equilibrium structures at high density are fcc, a consequence of Kepler's conjecture. But finite packings of such particles, as found in isolated clusters, complexes, or local arrangements of bulk phases, frequently

¹Department of Chemical Engineering, ²Department of Materials, University of California, Santa Barbara, CA 93106, USA.

*To whom correspondence should be addressed. E-mail: pine@mr.lucsb.edu

adopt point symmetries that are inconsistent with fcc order. For example, local polytetrahedral packings with fivefold symmetry are energetically favored in undercooled metallic liquids (5–7). The incompatibility of these packings with long-range order inhibits crystal nucleation and induces the formation of metastable phases (7). Similar arguments involving conflicting optimal packing criteria at the local and bulk scales are central to theories of glass formation (8) and jamming (9, 10). A better understanding of how finite groups of spheres organize themselves may therefore help us decipher and control the structure of matter at many different length scales. To this end, a primary scientific challenge is to determine the minimization principle that governs the shapes of finite packings for a given set of physical constraints.

We show that under a compressive force, small numbers ($n = 2$ to 15) of hard spheres pack into distinct and identical polyhedra for each value of n . These configurations (clusters) are related to a fundamental minimization principle that was only recently discovered within the mathematics literature (11). The clusters are formed in a three-phase colloidal system consisting of evaporating oil droplets suspended in water, with n micrometer-sized polymer spheres (microspheres) attached to the droplet surfaces. In this system, capillary forces provide a compressive force that is spherically symmetric until packing constraints break the symmetry. A key feature of our approach is that for a given value of n , the packing process is reproducible and can be examined dynamically. In addition, we are able to isolate clusters of a given n in macroscopic quantities, thus providing a new class of nonspherical colloidal particles with which dif-

ferent packing and crystallization motifs can be studied.

Packing process. The principal components of our packings are equal-sized, cross-linked polystyrene microspheres, 844 nm in diameter [2.5% polydispersity (12)], with sulfate groups covalently bonded to the surface (13). In pure water, the sulfate groups dissociate, charging the surfaces of the spheres and preventing van der Waals attractions from bringing them together. In an organic solvent such as toluene, which is a good solvent for polystyrene, the dissociation of sulfate groups is limited, but the van der Waals forces between the particles are much smaller than in water (14). The particles swell with the solvent and interact only through a short-ranged steric (entropic) repulsion. To a good approximation, they act as hard spheres (15).

To pack these spheres together, we use a system that contains both liquids (13). We disperse the spheres in toluene (Fig. 1A), add water, and mix to create an oil-in-water emulsion consisting of small droplets of toluene ranging from 1 to 10 μm in diameter (Fig. 1B). The particles are strongly bound to the droplet interfaces by surface tension (16). We preferentially evaporate the toluene from the system, forcing the hard-sphere-like particles in each droplet to pack together (Fig. 1C). As Fig. 1D shows, the critical feature of the evaporation process is a mechanically stable intermediate stage called a spherical packing, formed when the particles touch one another on the surface of the droplet. Removing more oil at this stage causes the droplet to deform, generating capillary forces that ultimately lead to a rapid (<33 ms) rearrangement of the particles. When the last of the toluene evaporates, the particles deswell, at

which point the interparticle van der Waals attractions increase and the particles stick to one another, forming a small colloidal aggregate. Capillary forces thus pack the particles into their final configuration while they act as hard spheres, and van der Waals forces subsequently cement the spheres together. A side effect of this packing method is that the surfaces of the particles on the outside of the cluster are exposed to water at an earlier stage of evaporation. The dissociation of surface charges on these outer particles prevents the cluster as a whole from aggregating with other clusters.

Geometry of microsphere packings. After all the toluene has evaporated, we are left with a suspension of clusters of different sizes. Each cluster comes from a single droplet containing n spheres, but n varies from cluster to cluster because the initial droplets are not uniform in size. Centrifugation in a density gradient (13) allows us to separate the clusters on the basis of differences in sedimentation velocity, or average hydrodynamic radius (17). Although all of our microspheres have the same mass, the effective surface area and the sedimentation velocity of a cluster of these particles vary greatly with their configuration. The separation yields a set of sharp, well-separated bands (Fig. 2), showing that only specific configurations emerge from our packing process.

In fact, the separation reveals a remarkable result: Clusters of a given n are all identical, as determined by extracting the bands from the density gradient (insets, Fig. 2) and examining the clusters with the optical microscope. The structures of the clusters are shown in Fig. 3. If we treat the center of each sphere as a vertex of a polyhedron, the first few observed configurations are the line seg-

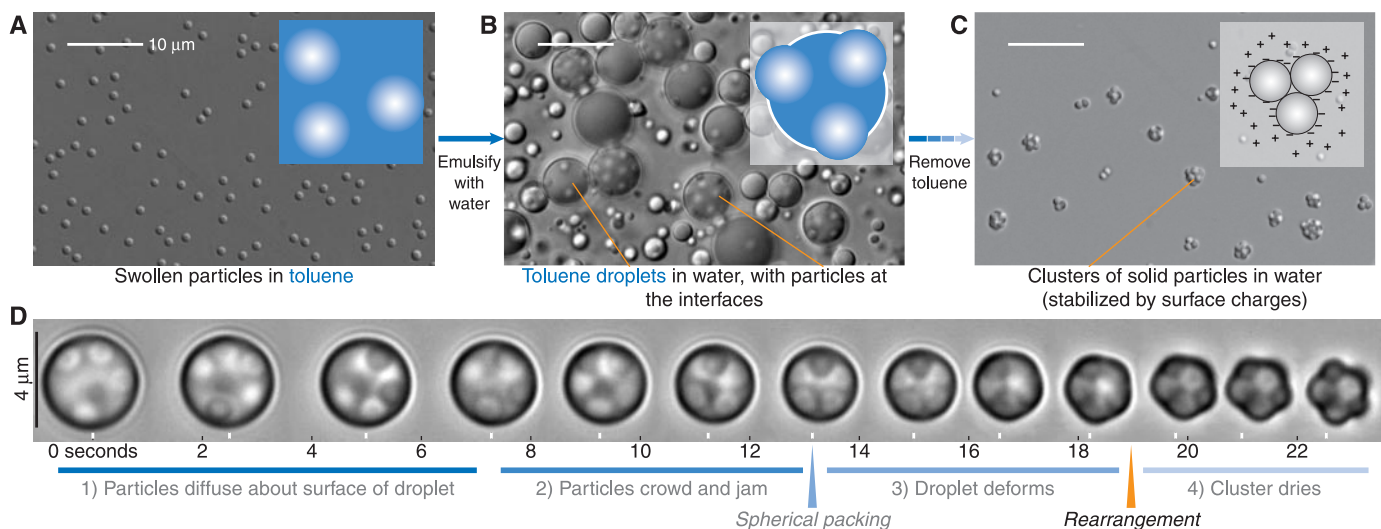


Fig. 1. Optical micrographs and diagrams (insets) of the packing process. (A) Polymer particles swollen and dispersed in toluene (shown in blue). (B) Emulsion of toluene droplets with particles, still swollen, bound to the interfaces. (C) Clusters after toluene evaporation. These are stabilized against further aggregation by the dissociation of charged groups on the surfaces of the particles. (D) A time series of micrographs taken during

evaporation of the toluene, showing the evolution of the system between (B) and (C). Particles freely diffuse about the surface of the droplet until, as more toluene evaporates, they touch one another, forming a spherical packing (blue arrowhead). Deformation of the interface then leads to a rapid rearrangement (orange arrowhead) to a cluster. The final configuration of this seven-sphere cluster is also shown in Fig. 3.

ment ($n = 2$), triangle ($n = 3$), tetrahedron ($n = 4$), triangular dipyrmaid ($n = 5$), and octahedron ($n = 6$). These familiar structures occur in many common molecules or coordination complexes. For example, these are the packings of fluorine atoms in diatomic fluorine, boron trifluoride, carbon tetrafluoride, phosphorus pentafluoride, and sulfur hexafluoride, respectively. The polyhedra are also subelements (local packings) of the fcc lattice or its stacking variants.

The larger clusters are an unusual and perhaps unfamiliar set of packings. None of these can be decomposed into combinations of regular tetrahedra and octahedra, and thus none is found in close-packed lattices. Clusters containing 7 to 10 particles are members of a set of highly symmetric polyhedra known as convex deltahedra (18), some of which belong to noncrystallo-

graphic point groups (see classifications in Fig. 3) such as D_{5h} (fivefold symmetry, $n = 7$) and D_{4d} ($n = 10$). Bernal (19) observed that these polyhedra cannot fill space, and proposed that they might represent local packings of atoms in liquid phases. Deltahedral geometry also occurs in certain boron hydride molecules (20), but this is a result of the trivalent bonding of boron rather than of a sphere-packing process. Compared to the deltahedral packings, the 11-sphere cluster is particularly striking, as it is the lowest- n cluster that is not convex. It belongs to the low-symmetry point group C_s .

Atoms interacting through a spherically symmetric Lennard-Jones potential form clusters similar to ours up to $n = 7$ (21), but for $n > 7$ Lennard-Jones clusters minimize energy by maximizing the number of contacts between particles, which leads to polytetrahedral packings. Although our seven-sphere cluster can be viewed as an aggregate of five distorted tetrahedra (22), the other clusters are not polytetrahedral, and they generally have higher symmetry than the Lennard-Jones packings. Overall, the sequence of sphere packings we obtain is distinct from others observed in matter.

The unique structures of the packings for each n suggest that they are optimal arrangements in the context of some minimization principle. The simplest candidate for minimization is the potential energy. In our system, though, the only attractive interactions are the van der Waals forces that bind the particles together. These short-ranged interactions are insignificant compared to the thermal energy when the distance between the sphere surfaces is greater than about 50 nm, given a Hamaker constant of 10^{-20} J for the polystyrene-water-polystyrene system (23). Thus, if van der Waals forces were responsible for the clustering, we would expect the clusters to adopt the structures of Lennard-Jones clusters. They do not, implying that our packings are not a result of attractive forces.

The clusters do not minimize their volume either, at least not for any simple definition of volume. Minimizing the volume of the convex hull of a set of spheres leads to a sequence of clusters known as sausage packings, or linear arrangements of spheres for $n < 56$ (24, 25). Minimizing the volume of the smallest spherical hull that encapsulates the particles leads to a different set of packings as well (26).

Because attractions do not cause the clustering and because density cannot be precisely defined for our packings, we examine the next simplest quantity to minimize: the second moment of the mass distribution $M_2 = \sum_{i=1}^n |\mathbf{r}_i - \mathbf{r}_0|^2$, where \mathbf{r}_i is the center coordinate of the i th sphere and \mathbf{r}_0 is the center of mass of the cluster. Minimizing the second moment is perhaps the most conve-

nient way to define density without resorting to artificial definitions of cluster volume. Using global optimization techniques, Sloane *et al.* (11) have calculated the packings that minimize M_2 (minimal-moment packings), obtaining a sequence of clusters with unique configurations for each n . These theoretical configurations exactly correspond to those of our packings (Fig. 3A). Although the minimization principle is quite fundamental, we know of no observations of this type of packing in nature.

Relation between cluster packings and spherical packings. In analyzing the mechanism by which the minimal-moment clusters form, we find that the essential element is the spherical packing: the shell of particles on the surface of the droplet that causes the interface to deform (stage three in Fig. 1D). After the spherical packing forms, Brownian motion no longer plays a role in the development of the cluster, because capillary and contact forces now move the particles. The final cluster configurations are thus determined solely by the positions of particles in the spherical packing. At this stage, there is a well-defined density: the number of particles per unit of surface area. We believe each n -sphere cluster is identical because each n -particle droplet system must proceed through a spherical packing that maximizes this density. Our clusters may therefore represent collapsed states of optimal spherical packings. In this scenario, the second moment of the mass distribution is a reasonable quantity to minimize, because the capillary forces acting on the particles in the spherical packing are directed toward the center of the droplet.

The configurations of clusters with $n > 11$ support the notion of clusters as collapsed optimal spherical packings. The higher-order clusters are not minimal-moment clusters (Fig. 3B), although for $n = 12$ and $n = 13$ they differ only in the positions of one or two spheres. Our 12-sphere cluster is a pure icosahedron, a configuration that is known to have optimal spherical packing (27). Symmetry appears to prevent rearrangement in this case, because all sphere positions are indistinguishable, so there is no weak spot to initiate the collapse. However, when we dry suspensions of icosahedra completely, we do observe minimal-moment structures, likely because the higher surface tension of air-water interfaces, compared to that of toluene-water interfaces, leads to much greater capillary forces.

The spherical packings for 13 spheres and more do rearrange after oil evaporation, but they do not minimize the second moment. Compared to the lower-order clusters, a critical difference is that the minimal-moment structures contain an internal sphere, or a sphere coordinated fully by 12 others. In our system, the particles in the spherical packing

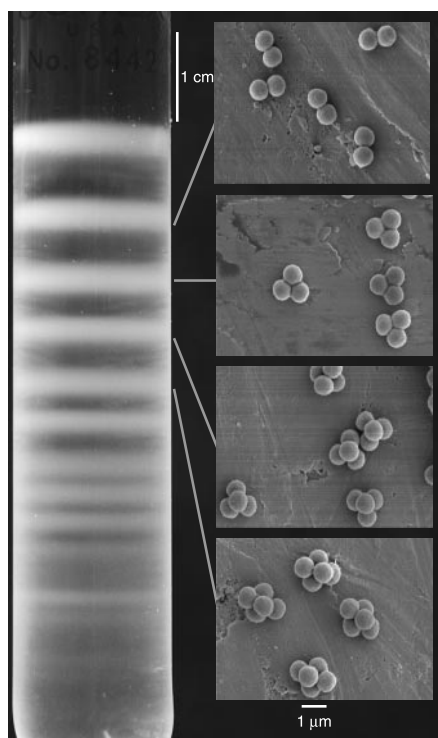


Fig. 2. Photograph of a test tube containing a cluster suspension separated by centrifugation in a density gradient (left). Fourteen distinct bands, each representing a region of high concentration of clusters, are visible in the tube, showing that the cluster formation process leads to specific, well-defined configurations of particles. The number and sharpness of the bands starkly contrast with those of fractally aggregated clusters (30), where increasing configurational variations prevent banding for $n > 3$. Each band shown contains clusters of the same n , with $n = 1$ at the top (see electron micrographs at right). Each of the upper bands contains between 10^8 and 10^{10} identical colloiddally stable clusters, making the separation process a useful method for preparing macroscopic suspensions of particles with various shapes.

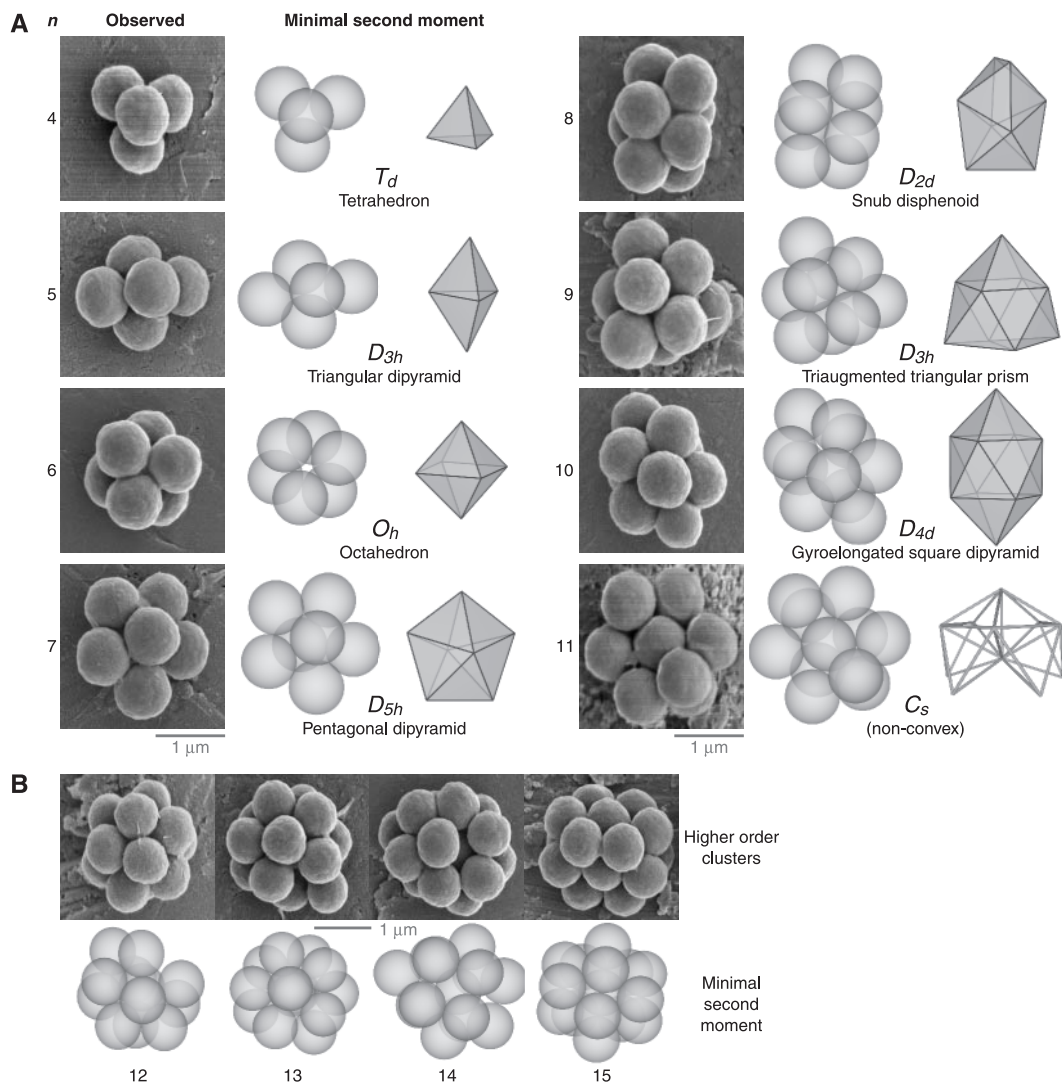


Fig. 3. Cluster configurations at each n , as determined by optical and electron microscopy. Some shrinkage and deformation of the spheres occur during drying and exposure to the electron beam, but the configurations of particles remain the same as those observed in situ optically. (A) Left columns show electron micrographs of the clusters. All clusters of a given n have identical structures. Right columns illustrate the polyhedra formed by drawing lines from the center of each particle to its neighbors. Below are the names of the polyhedra [from (78)] and Schönflies point groups. Middle columns show computer renderings of sphere configurations that minimize the second moment of the mass distribution (11), which match our packings. Not shown are the line segment ($n = 2, D_{\infty h}$) and the triangle ($n = 3, D_{3h}$). (B) Clusters with $n > 11$ differ increasingly from minimal second moment structures. We observe some small variations in the packing from cluster to cluster for $n > 12$.

are bound to a continuous and smooth surface, the droplet interface, and there does not appear to be a route to an internal sphere upon collapse. The second moment does, however, decrease in the rearrangement, and the configurations we observe are consistent at each n , albeit with many more small variations in the packing than at lower n . Minimization of higher-order moments, defined by $M_k = \sum_{i=1}^n |\mathbf{r}_i - \mathbf{r}_0|^k$, where k is any integer greater than 2, does not account for the $n > 12$ configurations. For these cases, M_k (at least up to $k = 7$) is smaller for the minimal second moment packings than for the packings we observe. For $n \leq 12$, minimization of higher moments appears to favor structures that are more isotropic, so that a spherical packing of eight spheres has a lower M_3 than our eight-sphere cluster, and a spherical packing of 11 spheres has a lower M_4 than our 11-sphere cluster. The second moment thus remains the most appropriate measure of density. Minimization of the second moment subject to a constraint (for example, that no internal spheres may exist) might account for

all the cluster configurations we observe. In any case, the configurations for $n > 11$ are an even more unusual set of packings, with a notable lack of symmetry for the 13- and 14-sphere clusters, both of which are chiral, and high symmetry for the 12-sphere (I_h point group) and 15-sphere (D_{3h}) clusters.

Colloidal dispersions of clusters. From a technological perspective, the salient feature of our process is that it consistently yields a specific set of structures with unique and interesting symmetries. We can exploit this feature using the separation procedure we describe above. In the density gradient tube shown in Fig. 2, there are billions (10^8 to 10^{10} , or 0.1 to 10 mg) of each type of cluster. Thus, by separating the bands, we can produce entire colloidal dispersions of sphere doublets, tetrahedra, or any of the larger, more exotic polyhedra in macroscopic quantities. These dispersions remain stable indefinitely, with no cluster breakup or intercluster aggregation. Static light-scattering measurements on dilute cluster suspensions show excellent agreement with rigorous calculations

of scattering from idealized sphere packings of the same symmetries (Fig. 4), indicating that each cluster fraction is stable and well separated. There are other methods for making colloidal clusters (28, 29), but because these rely on adsorption onto patterned substrates, they have intrinsically small yields (10^5 clusters) and require that the packings be constructed in a layer-by-layer fashion, which cannot reproduce all the structures shown here.

Concluding remarks. Our observations support the idea of the second moment of the mass distribution as a simple, useful definition of optimal packing in certain colloidal systems. This minimization principle may provide some insights into the local processes underlying the densification of bulk powder slurries or wet granular materials. Beyond these applications, though, lies a new role for colloidal microspheres: as model systems for studying packing itself. Optimal finite sphere packings are still poorly understood mathematically and scientifically, and even our relatively simple system produces a sequence of packings predicted only within the past dec-

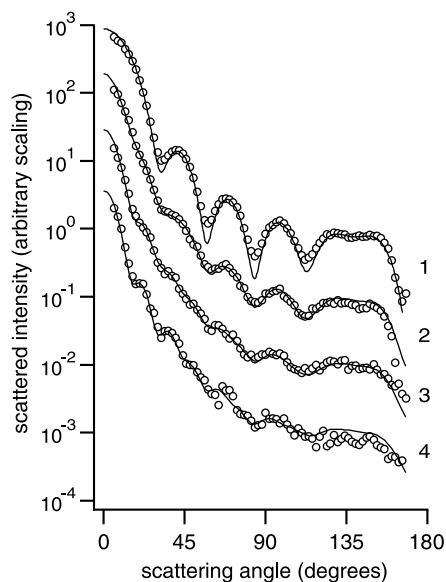


Fig. 4. Intensity of scattered light (488 nm) as a function of scattering angle for dispersions of the first four clusters. Solid lines are calculations of the theoretical scattering from randomly oriented idealized packings of 844-nm spheres (31). The data and curves are offset for clarity. Curve 1, single spheres; 2, sphere doublets; 3, triangles; 4, tetrahedra. The agreement between theory and experiment shows that the clusters are well separated and stable.

ade (11). The varied and unusual polyhedra of this sequence illustrate how certain symmetries, including fivefold rotational symmetry, can arise solely from compression and packing constraints and need not require interparticle attractions. It may well be possible to define other types of constraints in microsphere systems and in so doing to discover new sphere-packing motifs.

References and Notes

- J. H. Conway, N. J. A. Sloane, *Sphere Packings, Lattices, and Groups* (Springer, New York, ed. 3, 1999).
- T. C. Hales, *Discrete Comput. Geom.* **17**, 1 (1997).
- T. C. Hales, *Discrete Comput. Geom.* **18**, 135 (1997).
- L. Fejes-Tóth, *Regular Figures* (Macmillan, New York, 1964).
- H. Reichert *et al.*, *Nature* **408**, 839 (2000).
- T. Schenk, D. Holland-Moritz, V. Simonet, R. Bellissent, D. M. Herlach, *Phys. Rev. Lett.* **89**, 075507 (2002).
- K. F. Kelton *et al.*, *Phys. Rev. Lett.* **90**, 195504 (2003).
- D. R. Nelson, F. Spaepen, *Solid State Phys.* **42**, 1 (1989).
- A. J. Liu, S. R. Nagel, *Nature* **396**, 21 (1998).
- C. S. O'Hern, S. A. Langer, A. J. Liu, S. R. Nagel, *Phys. Rev. Lett.* **86**, 111 (2001).
- N. J. A. Sloane, R. H. Hardin, T. D. S. Duff, J. H. Conway, *Discrete Comput. Geom.* **14**, 237 (1995).
- Polydispersity is defined as the relative standard deviation in the particle size distribution.
- Materials and methods are available as supporting material on Science Online.
- B. R. Saunders, B. Vincent, *Adv. Colloid Interface Sci.* **80**, 1 (1999).
- M. S. Wolfe, C. Scopazzi, *J. Colloid Interface Sci.* **133**, 265 (1989).
- S. Levine, B. D. Bowen, S. J. Partridge, *Colloids Surf.* **38**, 325 (1989).
- R. Hinton, M. Dobrota, *Density Gradient Centrifugation*, vol. 6, part 1, of *Laboratory Techniques in Bio-*

- chemistry and Molecular Biology* (Elsevier/North-Holland, New York, 1976).
- N. W. Johnson, *Can. J. Math.* **18**, 169 (1966).
 - J. D. Bernal, *Nature* **185**, 68 (1960).
 - R. E. Williams, *Inorg. Chem.* **10**, 210 (1971).
 - M. R. Hoare, P. Pal, *Adv. Phys.* **20**, 161 (1971).
 - F. Spaepen, *Nature* **408**, 781 (2000).
 - R. Hidalgo-Álvarez *et al.*, *Adv. Colloid Interface Sci.* **67**, 1 (1996).
 - U. Betke, M. Henk, J. M. Wills, *Discrete Comput. Geom.* **13**, 297 (1995).
 - J. M. Wills, *Math. Intell.* **20**, 16 (1998).
 - A. Boerdijk, *Philips Res. Rep.* **7**, 303 (1952).
 - B. W. Clare, D. L. Kepert, *Proc. R. Soc. London Ser. A* **A405**, 329 (1986).
 - J. Aizenberg, P. V. Braun, P. Wiltzius, *Phys. Rev. Lett.* **84**, 2997 (2000).

- Y. D. Yin, Y. N. Xia, *Adv. Mater.* **13**, 267 (2001).
- M. M. Takayasu, F. Galembeck, *J. Colloid Interface Sci.* **202**, 84 (1998).
- D. W. Mackowski, M. I. Mishchenko, *J. Opt. Soc. Am. A* **13**, 2266 (1996).
- We thank V. Breedveld and D. Roux for helpful discussions. Supported by NSF under grant numbers CTS-0221809 and DGE-9987618 and by Unilever Corporation.

Supporting Online Material

www.sciencemag.org/cgi/content/full/301/5632/483/DC1

Materials and Methods
References

28 April 2003; accepted 18 June 2003

Cell Therapy of α -Sarcoglycan Null Dystrophic Mice Through Intra-Arterial Delivery of Mesoangioblasts

Maurilio Sampaolesi,¹ Yvan Torrente,² Anna Innocenzi,¹
Rossana Tonlorenzi,¹ Giuseppe D'Antona,³
M. Antonietta Pellegrino,³ Rita Barresi,⁴ Nereo Bresolin,^{2,5}
M. Gabriella Cusella De Angelis,^{1,3} Kevin P. Campbell,⁴
Roberto Bottinelli,³ Giulio Cossu^{1,6,7*}

Preclinical or clinical trials for muscular dystrophies have met with modest success, mainly because of inefficient delivery of viral vectors or donor cells to dystrophic muscles. We report here that intra-arterial delivery of wild-type mesoangioblasts, a class of vessel-associated stem cells, corrects morphologically and functionally the dystrophic phenotype of virtually all downstream muscles in adult immunocompetent α -sarcoglycan (α -SG) null mice, a model organism for limb-girdle muscular dystrophy. When mesoangioblasts isolated from juvenile dystrophic mice and transduced with a lentiviral vector expressing α -SG were injected into the femoral artery of dystrophic mice, they reconstituted skeletal muscle in a manner similar to that seen in wild-type cells. The success of this protocol was mainly due to widespread distribution of donor stem cells through the capillary network, a distinct advantage of this strategy over previous approaches.

There are currently three main experimental approaches to therapy of muscular dystrophies (1). Gene therapy focuses on the development of new vectors capable of delivering

efficiently the missing gene to the postmitotic nuclei of the muscle fibers in vivo. The pharmacological approach aims to restore the protein complex that is altered in many forms of muscular dystrophy through different strategies ranging from skipping mutated exons to increasing the synthesis of cognate proteins such as utrophin. The cell therapy approach aims to functionally rescue the tissue by delivery of cells (2); these may be satellite cells (which regenerate new fibers after damage to the muscle) or pluripotent stem cells (which have been shown to differentiate into skeletal muscle both in vitro and in vivo). However, the limited self-renewal and migratory capacity of dystrophic satellite cells and our modest knowledge of stem cell biology have so far hampered the success of the cell therapy approach.

We recently identified a class of vessel-associated fetal stem cells that can differ-

¹Stem Cell Research Institute, H. S. Raffaele, Via Olgettina 58, 20132 Milan, Italy. ²Department of Neurological Science, Istituto di Ricovero e Cura a Carattere Scientifico (IRCCS), Centro Dino Ferrari, Ospedale Maggiore Policlinico, Via F. Sforza 35, 20122 Milan, Italy. ³Department of Experimental Medicine, University of Pavia, Via Forlanini 6, 27100 Pavia, Italy. ⁴Howard Hughes Medical Institute, Department of Physiology, Biophysics and Neurology, University of Iowa College of Medicine, Iowa City, IA 52242, USA. ⁵IRCCS E. Medea, Bosisio Parini, 23842 Lecco, Italy. ⁶Department of Histology and Medical Embryology, University of Rome "La Sapienza," Via A. Scarpa 14, 00161 Rome, Italy. ⁷Institute of Cell Biology and Tissue Engineering, San Raffaele Biomedical Science Park of Rome, Via Castel Romano 100, 00128 Rome, Italy.

*To whom correspondence should be addressed. E-mail: cossu.giulio@hsr.it